AGU PUBLICATIONS

JGR

Journal of Geophysical Research: Space Physics

RESEARCH ARTICLE
10.1002/2017JA024364

Key Points:
- During the April 2010 geomagnetic storm, direct production of nitric oxide is observed down to 55 km in the polar atmosphere
- The main nitric oxide number density variability at 55 km is seen 15 days after storm onset and is caused by the indirect effect
- The source region for descending nitric oxide is in the upper mesosphere (~75–90 km), associated with medium-energy electrons (>10 keV)

Correspondence to:
C. Smith-Johnsen,
christine.smith.johnsen@gmail.com

Citation:
Smith-Johnsen, C., H. Nesse Tyssøy, K. Hendrickx, Y. Orsolini, G. Kishore Kumar, L.-K. G. Ødegaard, M. I. Sandanger, F. Stordal, and L. Megner (2017), Direct and indirect electron precipitation effect on nitric oxide in the polar middle atmosphere, using a full-range energy spectrum, *J. Geophys. Res. Space Physics*, *122*, 8679–8693, doi:10.1002/2017JA024364.

Received 15 MAY 2017
Accepted 5 JUL 2017
Accepted article online 12 JUL 2017
Published online 2 AUG 2017
Corrected 3 NOV 2017

This article was corrected on 3 NOV 2017. See the end of the full text for details.

Direct and indirect electron precipitation effect on nitric oxide in the polar middle atmosphere, using a full-range energy spectrum

Christine Smith-Johnsen[1], Hilde Nesse Tyssøy[2], Koen Hendrickx[3], Yvan Orsolini[2,4], Grandhi Kishore Kumar[2], Linn-Kristine Glesnes Ødegaard[2], Marit Irene Sandanger[2], Frode Stordal[1], and Linda Megner[3]

[1]Section for Meteorology and Oceanography (MetOs), University of Oslo, Oslo, Norway, [2]Birkeland Centre for Space Science, University of Bergen, Bergen, Norway, [3]Department of Meteorology (MISU), Stockholm University, Stockholm, Sweden, [4]Norwegian Institute for Air Research (NILU), Kjeller, Norway

Abstract In April 2010, a coronal mass ejection and a corotating interaction region on the Sun resulted in an energetic electron precipitation event in the Earth's atmosphere. We investigate direct and indirect nitric oxide (NO) response to the electron precipitation. By combining electron fluxes from the Total Energy Detector and the Medium Energy Proton and Electron Detector on the National Oceanic and Atmospheric Administration's Polar-orbiting Operational Environmental Satellites, we obtain a continuous energy spectrum covering 1–750 keV. This corresponds to electrons depositing their energy at atmospheric altitudes 60–120 km. Based on the electron energy deposition, taking into account loss due to photolysis, the accumulated NO number density is estimated. When compared to NO measured at these altitudes by the Solar Occultation for Ice Experiment instrument on board the Aeronomy of Ice in the Mesosphere satellite, the NO direct effect was detected down to 55 km. The main variability at these altitudes is, however, dominated by the indirect effect, which is downward transported NO. We estimate the source of this descending NO to be in the upper mesosphere at ~75–90 km.

1. Introduction

Energetic electron precipitation (EEP) refers to accelerated electrons originating from the Sun or the magnetosphere which, guided by the Earth's magnetic field, enter the atmosphere at polar latitudes. The incoming energetic electrons will deposit their energy by ionization, dissociation, or excitation in the mesosphere and lower thermosphere (MLT) region, which in turn can lead to production of NO_x (NO and NO_2) and HO_x (OH and HO_2) [*Sinnhuber et al.*, 2012, and references therein]. In the MLT, NO is the dominant NO_x species which is, next to CO_2, one of the main constituents impacting the heat balance in the lower thermosphere [*Mlynczak et al.*, 2014]. Conversion to NO_2 occurs mostly below 70 km. Because of its lifetime of 1 day in sunlit conditions [*Brasseur and Solomon*, 2005], NO can be transported both horizontally and vertically by the background winds and waves.

Compositional changes brought by the EEP-induced production of NO_x at a specific altitude level are called the direct effects, while those caused by the vertical transport of NO_x are referred to as the indirect effects of EEP [*Randall et al.*, 2007]. In the stratosphere the NO_x lifetime increases, with a lifetime of the order of 1 month during the dark polar winter [*Brasseur and Solomon*, 2005]. The dynamics in the polar winter MLT region are dominated by the polar vortex and the downwelling within, which transports NO_x from the lower thermosphere and upper mesosphere into the stratosphere. In the stratosphere NO_x can lead to ozone destruction in the presence of sunlight, potentially causing a perturbation of the temperature, and in turn the large-scale atmospheric circulation. The indirect effect is particularly important during perturbed dynamical conditions, for example, sudden stratospheric warming events, when the downwelling is amplified following the vortex and stratopause reformation [*Meraner and Schmidt*, 2016; *Orsolini et al.*, 2017; *Holt et al.*, 2013].

Typically, there are two types of solar wind drivers for geomagnetic storms: corotating interaction regions (CIRs) associated with high-speed solar wind streams and coronal mass ejections (CMEs) associated with dense transient solar wind flows [*Richardson and Cane*, 2010; *Tsurutani and Gonzalez*, 1997; *Gonzalez et al.*, 1994].

CME-driven storms occur predominantly during solar maximum, while the CIRs make their largest contribution during the declining phase of the solar cycle.

The particle energy deposition in the MLT region and the in situ NO production is dependent on the type of the incoming particles and their associated energy. While the influence of the infrequent solar proton events on NO has been widely explored, the effect of the more frequent EEP events is still unresolved [*Rozanov et al.*, 2012; *Randall et al.*, 2015].

In this context, it is important to determine at which altitude the direct NO production occurs. There is limited evidence for in situ production of NO due to EEP below ~90 km [*Sinnhuber et al.*, 2012]. For the northern high latitudes, *Renard et al.* [2006] reported large increase in upper stratospheric NO_2 observed with Michelson Interferometer for Passive Atmospheric Sounding (MIPAS), attributed to a geomagnetic storm driven by coronal mass ejection (CME) in January 2004. This was repudiated by *Funke et al.* [2007] which attributed the same NO_2 increase to downward transport of upper mesospheric and lower thermospheric NO_x produced by auroral electrons. This conclusion is further supported by *Seppälä et al.* [2007] which used Global Ozone Monitoring by Occultation of Stars (GOMOS) NO_2 measurements to investigate the cause of the descending NO_x through the 2003/2004 winter. However, they also suggested that a geoeffective corotating interaction region (CIR) storm occurring in mid-February 2004 caused further enhancement, adding to the NO_x that was already descending. This was further investigated and corroborated by *Clilverd et al.* [2009]. At altitudes of 50–70 km the NO_2 increase, observed by GOMOS, was found to be consistent with the increase in the flux of relativistic electrons measured by the Geostationary Operational Environmental Satellites (GOES) as well as Polar-orbiting Operational Environmental Satellites (POES). This conclusion has also been questioned as measurements from MIPAS covering the same altitude and latitude region did not show evidence of an additional NO_2 source for the same period [*López-Puertas et al.*, 2006; *Sinnhuber et al.*, 2011]. *Sinnhuber et al.* [2014] could not fully rule out direct local NO production by EEP in the winter 2003/2004 but estimated it to be lower than 6 ppb in the altitude range 56–64 km.

Newnham et al. [2011] investigated a period of geoeffective CIR events at high southern latitudes in March and April 2008 using a ground-based passive microwave radiometer. They found that electrons of ~300 keV could account for the observed NO enhancement at 70–80 km. The data did not show evidence of downward descent from higher altitudes. Using the same instrument, *Daae et al.* [2012] indicate a direct effect down to 65 km in the Southern Hemisphere (SH) during a July 2009 moderate geomagnetic storm. *Hendrickx et al.* [2015] investigated the impact of the 27 day solar cycle in both hemispheres on NO production. They applied a superposed epoch analysis on measurements of NO by the Solar Occultation for Ice Experiment (SOFIE) instrument on board the Aeronomy of Ice in the Mesosphere (AIM) satellite. As a proxy for electron precipitation, they used the auroral electrojet (*AE*) index. They concluded that the direct NO production (on day 1 of the epoch analysis) can be observed down to about 90 km altitude, while an NO increase progressively propagated lower down in wintertime, approximately reaching 60 km over 2 weeks. *Kirkwood et al.* [2015] studied a series of recurring EEP events during Antarctic fall and winter 2010 using NO observations from the submillimeter microwave radiometer on the Odin spacecraft and statistical electron measurements from the Medium Energy Proton and Electron Detector (MEPED), on board POES. They observed NO enhancements up to 10 days after the events between 70 and 95 km and concluded that this resulted from both direct NO production and downward transport. They also concluded that below 85 km direct production contributes to a significant proportion of the mean enhancement but is too low to be detected for individual events.

The opposing results of the many studies mentioned show that the relative contribution of the direct production and indirect effect of NO in the mesosphere remains unanswered. This is partly due to inadequate particle measurement, as no single particle detector is able to measure both auroral and relativistic electrons at the same time, as well as the relative scarcity of NO observations over the polar MLT region. Lower production rates in the mesosphere make it difficult to determine the direct EEP impact since smaller in situ enhancements cannot be easily distinguished from the descending NO-rich air masses in the winter hemisphere [*Siskind and Russell*, 1996; *Funke et al.*, 2005; *Randall et al.*, 2007; *Sinnhuber et al.*, 2014].

We investigate the NO response in the SH during the geomagnetic storm in April 2010. The storm was driven by a combination of CME and a CIR, which causes significant enhancement in both the low- and high-energy electron fluxes. This event was chosen due to the high count of relativistic electrons measured by MEPED, and we expect to see an atmospheric response to this event throughout the MLT region. We estimate a full-range electron spectrum, impacting both the mesosphere and lower thermosphere by combining electron

measurement from the Total Energy Detector (TED) and MEPED particle detectors on the multiple POES spacecraft. To assess both the local production of NO throughout the MLT region and evaluate the contribution of the NO indirect effect, we monitor the NO response in this wide altitude range with the SOFIE instrument on board the AIM satellite. With a high vertical and temporal resolution, we can determine how deep in the atmosphere the NO direct effect can be detected and assess the relative importance of the direct and indirect NO enhancement throughout the event.

The paper is organized into section 2, followed by a description of the event presenting how the various parameters respond to the geomagnetic storm. In section 4 we disentangle the direct NO production from the transported NO based on our calculations and observations. The findings are then compared to previous studies. Section 5 summarizes our findings and their implications.

2. Instrumentation and Methods

2.1. TED and MEPED Detectors on the POES Satellites

NOAA (National Oceanic and Atmospheric Administration) has since the 1960s been operating the Polar-orbiting Operational Environmental Satellite (POES) series, and since 2006, EUMETSAT (European Organisation for the Exploitation of Meteorological Satellites) has been operating the MetOp (Meteorological Operational) satellites. In the period of interest in March/April 2010, six satellites were operational: NOAA 15 (1998 to present), NOAA 16 (2001–2014), NOAA 17 (2002–2013), NOAA 18 (2005 to present), MetOp-02 (2006 to present), and NOAA 19 (2009 to present). The spacecraft are orbiting at ~850 km altitude with a period of approximately 100 min and are equipped with instruments measuring the particle environment in the Earth's magnetosphere.

Each spacecraft carries two types of particle detectors, the Total Energy Detector (TED) and Medium Energy Proton and Electron Detector (MEPED). TED includes two electron detectors viewing at 0° and 30° to the local vertical. It measures low-energy electron fluxes in the energy range 0.05–20 keV, with read out of four differential electron energy bands 0.154–0.224 keV, 0.688–1.000 keV, 2.115–3.075 keV, and 6.503–9.457 keV. MEPED measures high-energy integral electron fluxes at >40, >100, and >300 keV and proton fluxes in six energy ranges from 30 to 6900 keV and >6900 keV [*Ødegaard et al.*, 2017]. It consists of two electron and two proton telescopes, pointing approximately 0° and 90° to the local vertical.

At middle and high latitudes the 0° telescopes measure particle fluxes that will be lost to the atmosphere, whereas the 30° and 90° telescopes might detect precipitating particle fluxes and/or trapped particles in the radiation belts. Here we use only the 0° telescopes which will provide a lower limit of the electron precipitation in the case of anisotropic pitch angle distribution [*Nesse Tyssøy et al.*, 2016]. The electron detectors are known to be contaminated by protons [*Evans and Greer*, 2000; *Yando et al.*, 2011]. In order to correct for the false counts due to proton contamination, we use the proton flux measurement from the proton telescopes as described in *Nesse Tyssøy et al.* [2016]. The protons have already been corrected due to detector degradation [*Sandanger et al.*, 2015; *Ødegaard et al.*, 2016]. We also account for the relativistic (>~750 keV) electrons contaminating the proton detector [*Nesse Tyssøy et al.*, 2016; *Ødegaard et al.*, 2017].

The corrected data set gives us a full-energy range coverage of electron energies that will be deposited in the MLT region. The six spacecraft are equipped with almost identical instruments which enable us to construct global maps of the precipitating electrons with high spatial and temporal resolution.

2.2. SOFIE Instrument on the AIM Satellite

NASA's Aeronomy of Ice in the Mesosphere (AIM) satellite was launched in May 2007 and is measuring properties of the mesosphere and lower thermosphere in order to study the variability in noctilucent clouds and their link to climate change. AIM has a polar, Sun-synchronous orbit with a period of 96 min. The Solar Occultation For Ice Experiment (SOFIE) instrument on board AIM performs solar occultation measurements to retrieve vertical profiles of NO, among other chemical species [*Gordley et al.*, 2009]. The NO is retrieved up to 150 km, with a vertical resolution of 2 km.

SOFIE is performing measurements two times for each of AIM's orbits: during sunset and sunrise. Because of AIM's retrograde orbit, all 15 measurements in the SH are made during local sunrise and all measurements in the Northern Hemisphere (NH) are made during local sunset. In the period of interest for this study, March/April 2010, the sunrises are at geographical latitudes between 72 and 82°S and the sunsets between 74 and 84°N. In corrected geomagnetic (CGM) latitude, the coverage in the NH is mostly poleward of the

auroral oval. In the SH AIM's orbit has a better coverage of the CGM latitudes, looking both outside and within the auroral oval throughout the entire event. We therefore limit our study to the SH. Summertime observations by SOFIE can be contaminated by water at altitudes below 80 km (M. Hervig, personal communication, 2016). During autumn and winter conditions there are low amounts of water in the mesosphere, so the NO observations during the April event in the SH are useful also in the mesosphere though with higher uncertainty in the absolute number densities.

In this paper, we will use a climatological mean of NO observations based on the period 2008–2012 not including 2010. By using the 2 years before and the 2 years after the event as climatology, we ensure that the sampling occurs in the same latitudinal area and limit influence from the varying solar cycle.

2.3. Methodology

The electron flux measured in specific energy channels is transformed to a continuous full-range energy spectrum, which is used to estimate an altitude profile of deposited energy and compared to SOFIE's NO profiles. The energy deposition profile is also used to estimate the production, accumulation, and depletion of NO when sunlight is taken into account. The following section explains the methodology in more detail.

On all six POES spacecraft, we use the electron flux measured for six energy channels: three with the TED instrument (centered at 0.844 keV, 2.595 keV, and 7.98 keV) and three from MEPED (78.5 keV, 203 keV, and 524 keV), based on the difference between four MEPED integral channels. During a period of 3 h, the different spacecraft are represented by 12 overpasses, as shown in Figure 1a. To account for poor satellite coverage between magnetic local time 10–14 in the SH, coincident measurements from one of the satellites in NH are also used here; see Figure 1b. This is necessary to avoid the interpolation of the high values from the morning sector, which would overestimate the EEP at those local times. The data mapped from the NH add a realistic low value. This confined interhemispheric mapping can be justified as the NH auroral oval is similar to the SH oval [*Hardy et al.*, 1985; *Laundal and Østgaard*, 2009]. The measurements are regridded into boxes with resolution 4° CGM latitude and 10° longitude (or 40 min in magnetic local time), as shown in Figure 1c. To construct a polar overview of the electron flux from each energy channel, this is interpolated linearly between the passes in a geomagnetic coordinate system. The resulting interpolated map is shown in Figure 1d. The interpolation is done in CGM coordinates but is then transformed to geographical coordinates with the same resolution, 4° latitude and 10° longitude; see Figure 1e.

The global maps in geographical coordinates of TED and MEPED electron energy fluxes (1–750 keV) are then combined to construct a continuous differential energy spectrum for each of the grid boxes. Previous studies apply a wide range of fits to various particle energy spectra. For example, *Kirkwood and Osepian* [2001] suggested an exponential form over the energy range 30–200 keV. *Rodger et al.* [2013] proposed a power law over the energy range 30–300 keV, and *Wissing and Kallenrode* [2009] apply five segments of power fit to TED and MEPED observations. For energies less than 10 keV, a Maxwellian or an exponential form is often applied. We find that a single spectra of neither exponential, Maxwellian, nor exponential form gives a good enough fit to the measurements over the wide-energy interval 1–750 keV. Therefore, we use either a Maxwellian or an exponential fit for the energies measured by TED, depending on the ratio between the first two channels: if channel 1 is higher than channel 2, an exponential fit is used, and if channel 2 is highest, we use a Maxwellian fit. The higher-energy fluxes are fitted with a power law spectrum. The transition from the exponential or Maxwellian fit and the power fit occurs around 30 keV. This combined curve fit is now a continuous differential energy spectrum. We use the cosine-dependent Isotropic over the Downward Hemisphere model from *Rees* [1989] to calculate the subsequent energy deposition as a function of altitude. This analysis is based on a standard reference atmosphere (COSPAR International Reference Atmosphere 1986). The altitude profile of the deposited energy, which has a time resolution of 3 h, can now be compared to the altitude profile of NO collocated in space and time with the SOFIE profiles.

The altitude profile of the deposited energy is also used to estimate the accumulation of NO. Starting out with a zero background of NO, we then estimate the NO locally produced by EEP during each 3 h time interval. With the energy deposition, we can get to the ionization rate assuming that the energy needed to create one ion pair is 35 eV. Each ion pair will produce 1.25 nitrogen atoms, where 0.7 is in the form N(2D) [*Jackman et al.*, 2005]. Assuming that all N(2D) is used to produce NO, we get the constant production rate for all altitude:

$$\text{NO produced} = \frac{\text{Energy deposited}}{35} * 0.7 \quad (1)$$

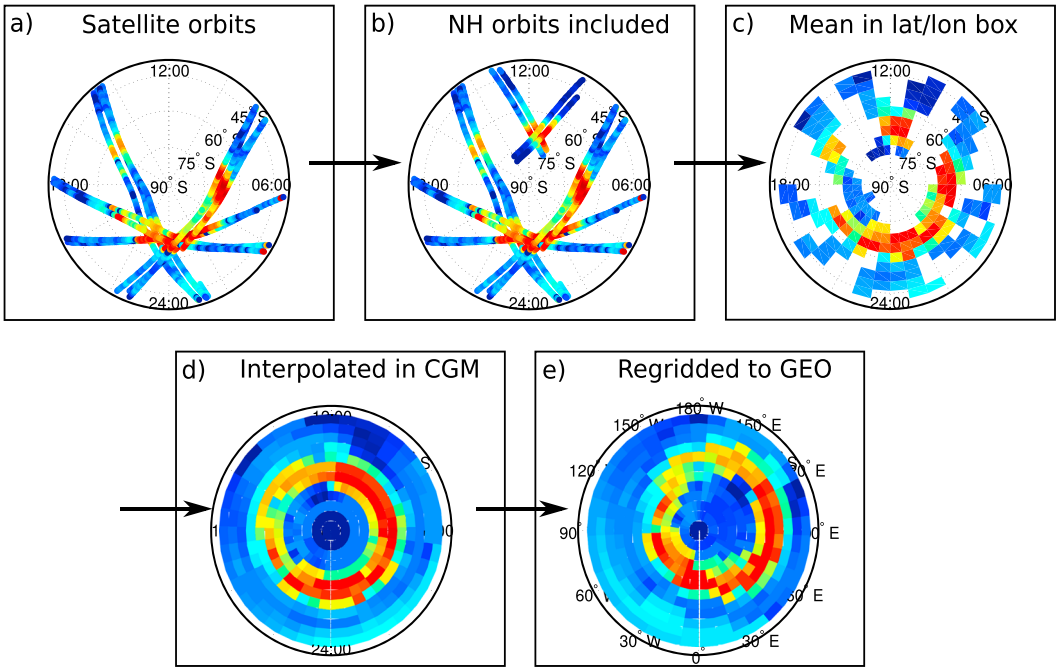

Figure 1. Stepwise description of how to get from POES' satellite tracks to a polar coverage of electron fluxes. (a) Electron flux from one energy channel, with 3 h resolution, shown in corrected geomagnetic latitude and magnetic local time for the SH. (b) Same as Figure 1a but with the conjugated electron flux from the NH mirrored down, in the magnetic local time region 10:00–14:00. (c) The electron fluxes gridded into 4° CGM latitude times 10° longitude boxes. (d) Interpolation of 3 h data to get a continuous coverage from poleward of 40°S CGM latitude. (e) The interpolated map of electron flux transformed to geographic coordinates, with same temporal and spatial resolution.

The assumption of a constant production rate is valid below 90 km, where the relation between N_2 and O_2 is fixed [*Verronen and Lehmann*, 2013]. In addition to production, there is also an NO loss by photolysis and from daylight chemistry started by photolysis. We first consider the angle between the Sun position and the selected geographic position. If the latter is in sunlit conditions, we assume a photolysis of 100% with a lifetime of a day [*Brasseur and Solomon*, 2005]. During twilight we assume 50% photolysis and 0% during total darkness. The resulting altitude profile of the accumulated NO is then compared to the SOFIE measurements of NO. Note that when estimating accumulated NO, we neglect horizontal and vertical transport; hence, this only shows an estimation of the local direct effect from EEP.

3. The April 2010 Energetic Electron Precipitation Event

3.1. Solar Wind and Geomagnetic Indices

Figure 2 shows solar wind parameters and geomagnetic indices for the time period considered. The first CME hits the Earth's magnetopause on the morning of 5 April (day of year (DOY) 95) [*Richardson and Cane*, 2017], followed by a steep solar wind speed increase associated with a CIR. The solar wind speed peaks at 800 km/s on DOY 95 and stays elevated (>500 km/s) for approximately 4 days (see Figure 2, first panel). The southward direction of the solar wind magnetic field makes the disturbance geoeffective, resulting in a negative deflection in the disturbance storm time (*Dst*) index of minimum −81 nT, classified as a moderate geomagnetic storm according to *Loewe and Prolls* [1997]. The recovery period is interrupted by a second CME on DOY 101 (11 April) which causes a second moderate geomagnetic storm period with *Dst* minimum −67 nT. The *Dst* also indicates some weak geomagnetic storms throughout our period of interest. In particular, the auroral electrojet (*AE*) index suggests auroral activity a few days prior (DOYs 91–92) to the first CME, as well as in the aftermath (e.g., DOYs 104 and 115) of the storm. The *AE* has a strong increase and reaches values as high as 1200 nT, suggesting that the main impact of the storm is likely to occur in the period DOYs 95–98, with a second disturbance also in accordance with the *Dst*.

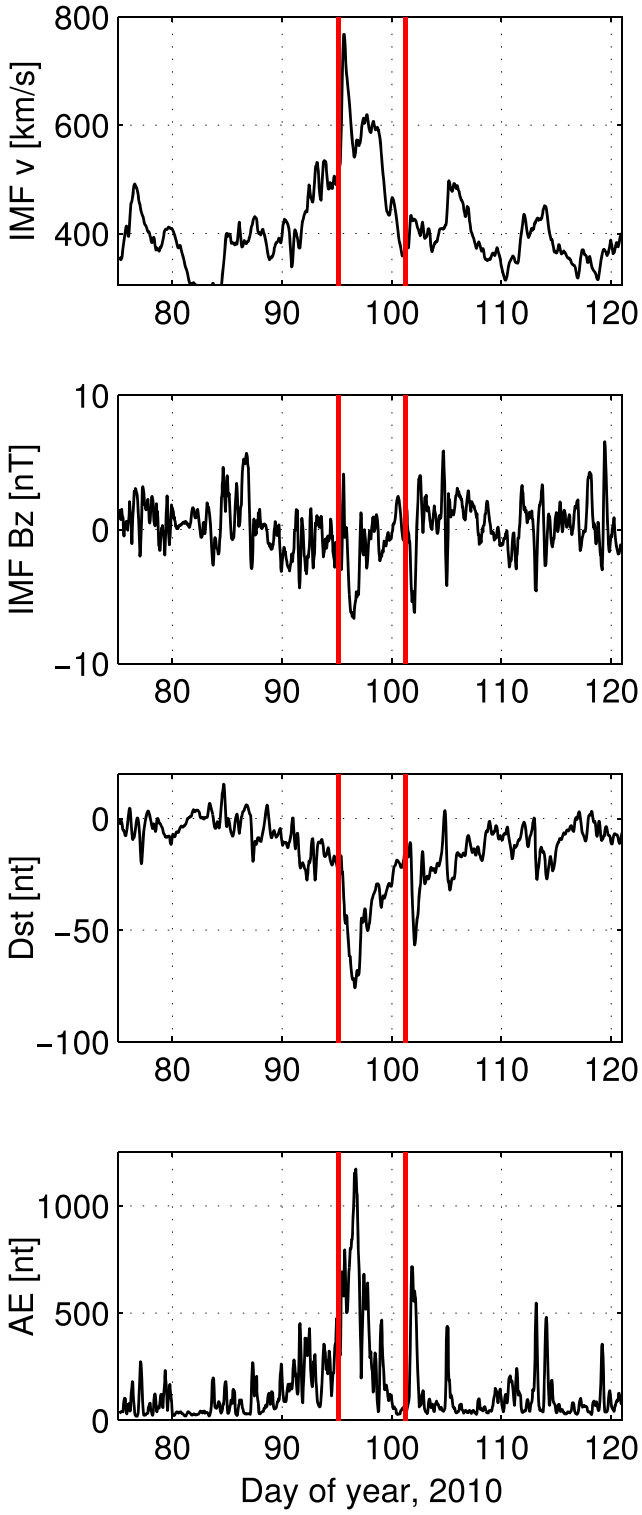

Figure 2. Hourly solar wind parameters and geomagnetic indices for the geomagnetic storm in April 2010. (a) Interplanetary magnetic field (IMF) velocity IMF *V* (km/s). (b) IMF north/south component, IMF B_z (nT). (c) The disturbance storm time (*Dst*) index (nT). (d) Auroral electrojet (*AE*) index (nT). The two red vertical lines indicate the time the CMEs hit the Earth's magnetopause [*Richardson and Cane*, 2017].

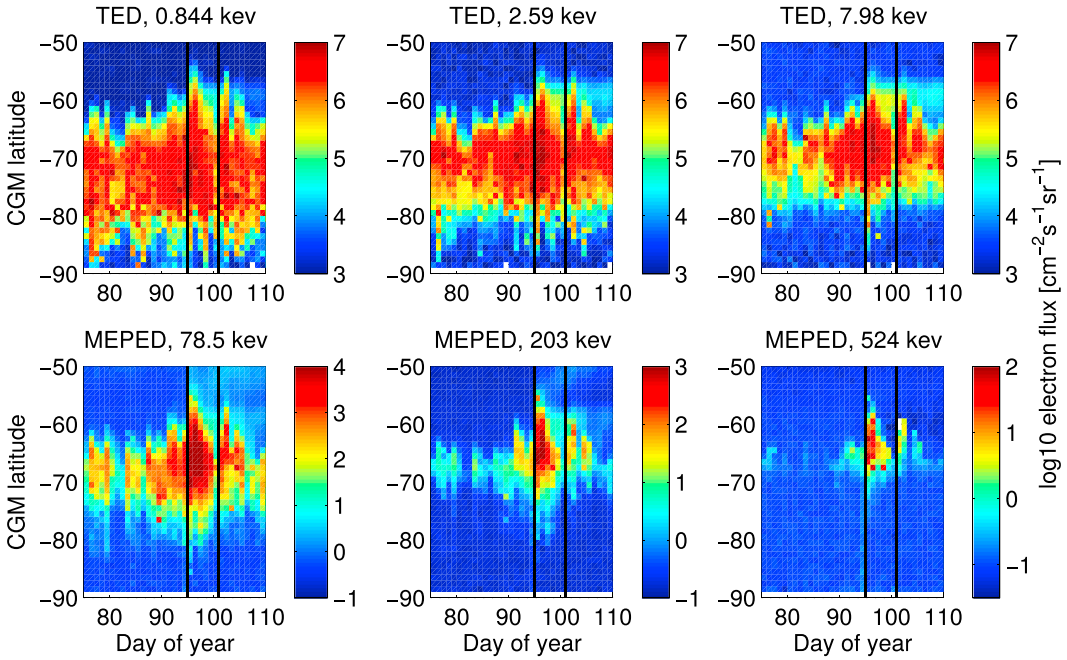

Figure 3. CGM latitude distribution over time of the electron fluxes from (top row) the three TED channels and (bottom row) the three MEPED channels on the POES satellites. The period shown is the EEP event in April 2010, for the SH. The two vertical lines highlight when the CMEs strike. Time resolution is 1 day, and latitude resolution is 1°.

3.2. Electron Fluxes Measured by POES

The electrons measured with the POES satellites are observed at different times and latitudes, depending on their energies. Figure 3 shows the CGM latitudinal distribution of the electron fluxes measured at the six energy channels during the April geomagnetic storm period. The lowest energy channel (centered at 0.844 keV) observes high fluxes of electrons at 65–85° CGM latitude and an equatorward movement of the peak flux at DOYs 95 and 101, when the two CMEs hit the Earth's magnetopause. The flux maximizes during the event by up to an order of magnitude, whilst the higher-energy channels suggest an increase of up to 2 orders of magnitude during the storm period. For the three higher-energy bands measured by MEPED, the flux is increasing at the start of the event (DOY 95) and expanding both poleward and equatorward during the storm period. The first CME gives the strongest increase of electron fluxes for all channels, both in terms of peak fluxes and latitudinal coverage.

3.3. Energy Deposition and Accumulated Nitric Oxide

High energetic electrons will penetrate deeper into the atmosphere than electrons with lower energies, and the associated ionization will result in increased production of nitric oxide. The increase in production also depends on the altitudinal profile of the background neutral density. The electron fluxes from POES are converted to altitude profiles of their deposited energy; see Figure 4 (left). Most of the energy from the incoming electrons is deposited above 90 km. One day after the first CME hits, the energy increase is evident all the way down to 55 km and lasting for about a day (DOY 96). For the second CME, the increase is seen only down to 80 km, also with 1 day delay and lasting for about 1 day (DOY 102).

The altitude profiles of the accumulated NO are shown in Figure 4 (right). The increase in accumulated NO starts at DOY 92, where the *AE* index shows increase of auroral activity and the low-energy electron channels observe a higher electron flux. The maximum is found in the 100–120 km altitude range, at DOYs 96–99 and 102–104, 1 day delayed from the two CMEs that hit the magnetopause. The accumulated NO at this altitude stays elevated throughout the geomagnetic storm period as more NO is produced when more energy is deposited, outweighing the photolytic loss. After the first CME, at DOY 96, a strong mesospheric increase is estimated reaching down to 55 km and lasting for about 3 days. At DOY 102, 1 day after the second CME, a new mesospheric increase occurs but this is not found below 80 km altitude.

3.4. Nitric Oxide Observations From SOFIE

Figure 5 (top and middle) shows how SOFIE's measurements of NO in the SH vary over time for the different altitudes and compares the events in 2010 to the same period for the years 2008–2009/2011–2012. The peak

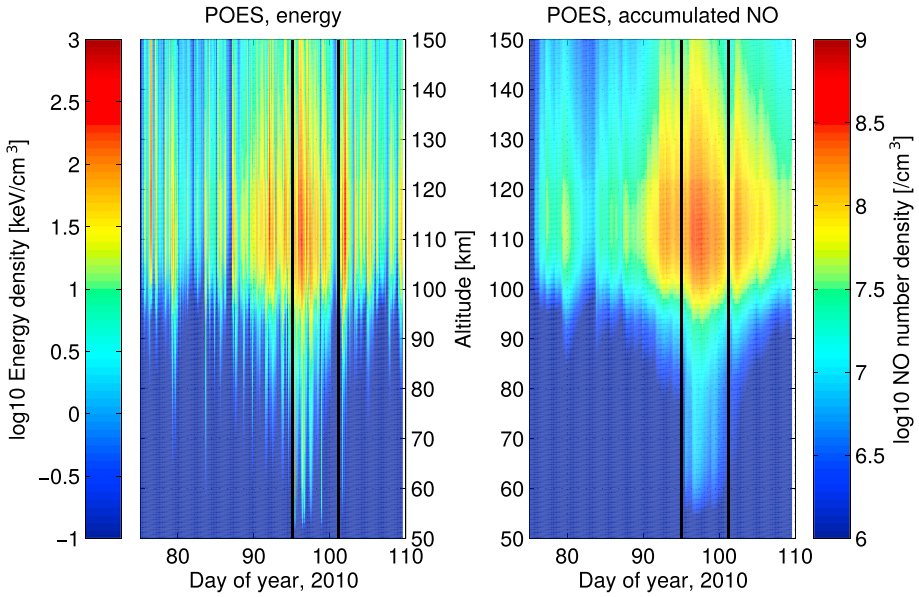

Figure 4. (left) Deposited energy for altitudes 50–150 km. Three hour time intervals and SH latitudes colocated with AIM-SOFIE's measurements. (right) Accumulated NO produced from the deposited energy and reduced due to Sun exposure. Three hour time intervals and SH latitudes colocated with AIM-SOFIE's measurements. The two CMEs are highlighted by the two vertical lines. Altitude resolution is 1 km for both panels.

(in number density) is found at 90–115 km altitude. Figure 5 (bottom) shows the relative difference between 2010 and the 2008–2009/2011–2012 climatology, with only positive increases above 1 sigma shown.

Above the NO main layer, at altitudes 115–140 km, the NO increase starts at about DOY 92. Then at the arrival of the CMEs (at DOYs 95 and 101, highlighted by black vertical lines), there is a reduction of NO lasting for about 2–3 days. After the CME arrivals the NO increases again, reaching 200% at DOYs 97–98 and almost a 100% increase at DOYs 103–104.

The NO increase is persistently highest at altitudes from 90 to 115 km, where we also see most of the energy deposited. Here the relative change reaches 300–400% of the climatological densities after the first CME at DOYs 96–99. A new peak in the NO increase occurs at DOYs 102–104, about a day after the second CME reaches Earth. The timing of both NO increases fits well with the accumulated NO shown in Figure 4. The anomalous high NO density does not persist longer than 4 days after the event onset from altitudes 100 and up to 130 km.

Below the main NO layer, i.e., below 90 km, and all the way down to 55 km, a positive change is found for all altitudes at DOY 96, 1 day after the first CME arrives. No increase can be seen before the event for these altitudes. The relative increase is highest at 55–60 km, which is due to the climatological low background at this altitude. Looking at the 2010 NO number density in Figure 5 (middle), a more continuous NO increase is seen for altitudes between 50 and 80 km. The NO increase fits well with the timing and altitude range of the increase in accumulated NO. An increase is also observed at 85 km at DOY 97, at 80 km at DOY 98, at 75 km at DOY 90 and all the way down to 50 km at DOYs 110–128. This is not seen in the accumulated NO, suggesting that the NO here has been transported down after being produced at a higher altitude.

Figure 6 shows the NO number density measured by SOFIE in altitude intervals from 55–65 km to 125–135 km, as function of CGM latitude. In the upper region, above the main NO layer, we find an increase starting some days before the geomagnetic storm starts and maximizing a few days after the first CME arrives. For altitudes 90, 100, and 110 km, the NO increase maximizes 1 day after the CME (at DOY 96). The increase can be seen strongest at CGM latitudes around 65–75°S, which corresponds well to the timing and location of where the electrons are coming in (see Figure 4 for the corresponding plot of electron distributed over time and CGM latitude). This concurrence in time and location between the EEP and NO suggests that the NO increase is due to direct production and not a product of transport. The days after DOY 96, the increase is also seen farther poleward of 75°S.

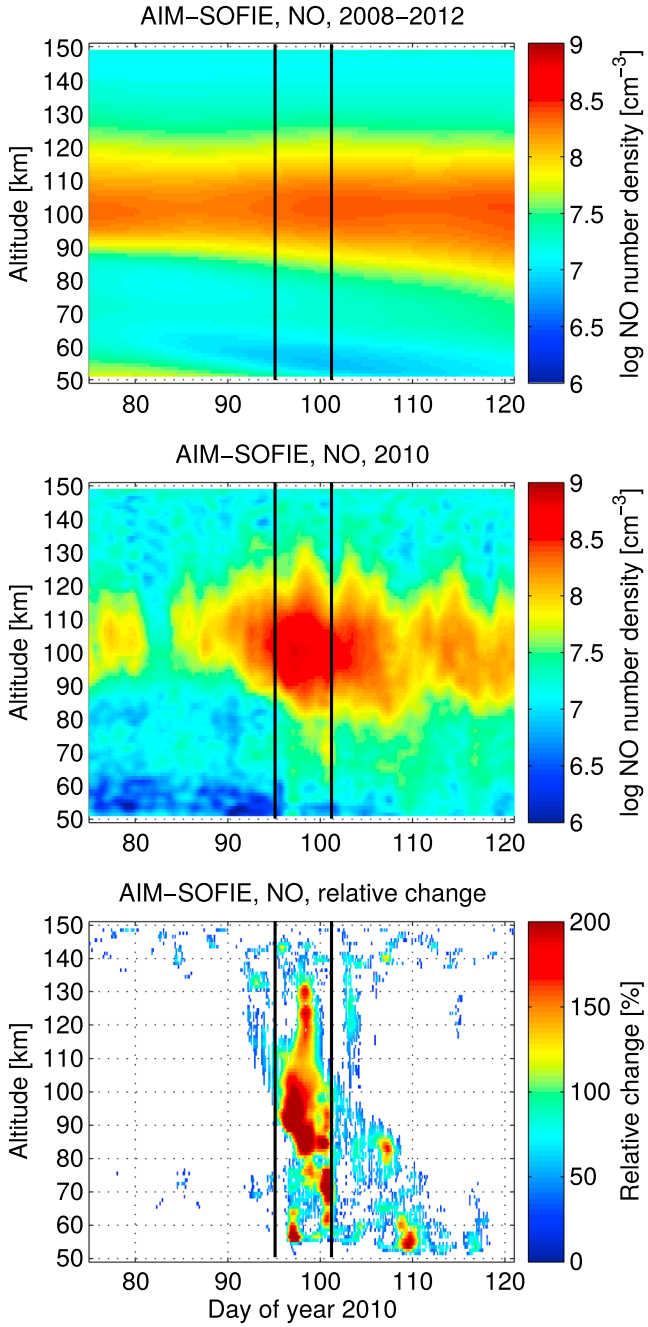

Figure 5. (top) AIM-SOFIE measurements of the altitude distributions of NO for the time period of day of year 85 until 120 as a climatological mean for the years 2008–2009/2011–2012. The arrival of the two CMEs is highlighted by black vertical lines. (middle) Same time period but for 2010 when the storm occurred. Three hour time resolution. (bottom) Percentage relative change in 2010 compared to climatology. Only positive change higher than one standard deviation of the climatology observations is shown.

For altitudes 80 and 70 km, an increase can be seen for CGM latitudes 65–75°S 1 day after onset of the first event, at DOY 96. The increase is strong and localized, indicating that it could be direct production. The increase of NO is also seen for the days after but more spread out in time and space. At 60 km the first increase is seen at DOY 96, followed by days with no increase, before a second increase is seen at DOYs 108–109. This second peak is more spread in time and covers all CGM latitudes observed, which could indicate that it has been transported both vertically and horizontally. The NO density increase is limited by the CGM latitudinal range of SOFIE's observations.

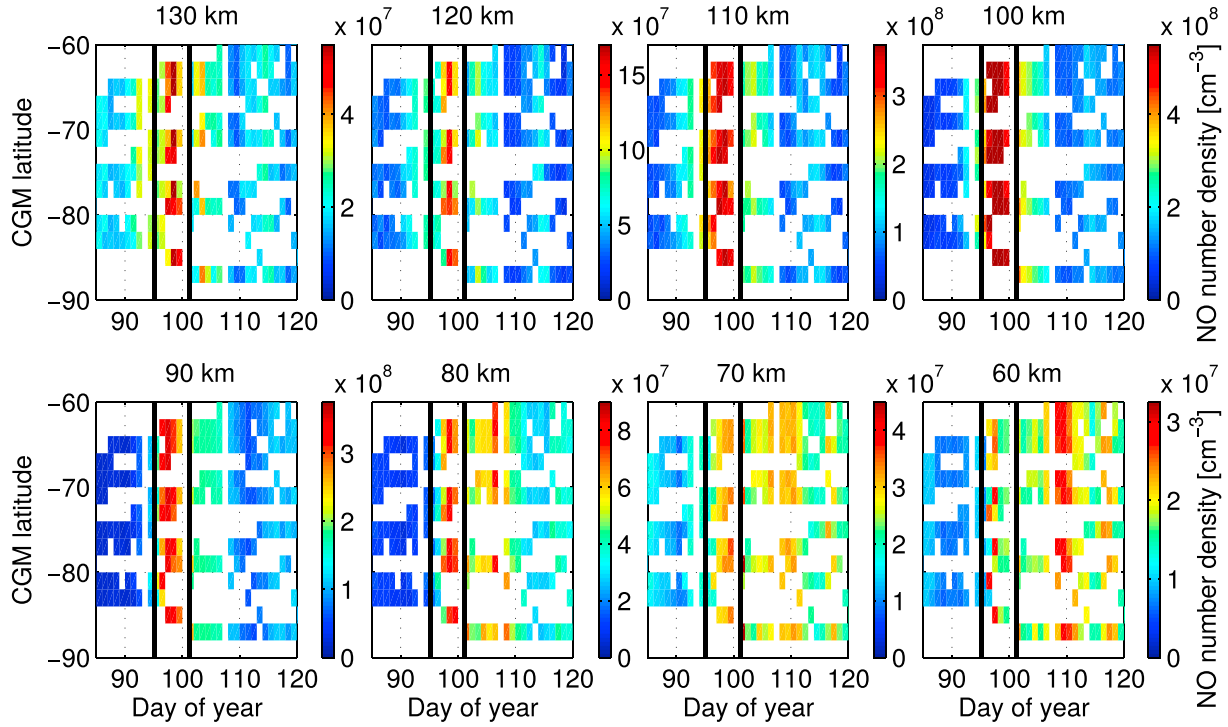

Figure 6. CGM latitude distribution of AIM-SOFIE measurements of NO in 2010, for eight altitude regions. Time resolution is 1 day, and the altitude is a 10 km mean. The arrivals of the two CMEs are highlighted by black vertical lines.

Comparing the April geomagnetic storm period to the other geomagnetic storms later in the 2010 Antarctic fall/winter, it seems to have a different signature, namely, faster NO descent. In Figure 7 we show the change of NO compared to the climatology for the SH from mid-February to the end of September 2010. We see an earlier NO increase at lower altitudes after the April storm than for the other EEP events during the SH winter of 2010. In the typical 2010 fall/winter events (excluding the April storm) the increase in NO at 55 km altitude is not seen until 25 days after the increase can be observed at 100 km. This indicates a downward transport of about 1.5–2 km/d. For the April event, however, we see the first increase at 90–115 km at DOY 96 and at 55 km already at DOY 97. A new increase at 55 km is seen after 15 days, indicating a downward transport of about 2.3 km/d.

3.5. Correlation Analysis

The satellite observations from SOFIE presented in the previous section show an increase of NO at the time of the two CMEs during the geomagnetic storm period in April 2010. This indicates a relation between the increase of NO and the incoming electrons.

Figure 8 (left) shows correlation of the SOFIE NO measurements to the colocated deposited energy estimated from TED/MEPED observations for the geomagnetic storm in April 2010. We correlate the relative change in NO in 2010 compared to the 2008–2012 climatology to exclude the seasonal effects. Different time delays between the energy and the NO measurements are introduced. At altitudes above 135 km, no consistent correlation is found. A positive significant correlation of 0.5 to 0.8 is found for all altitudes in the 85–135 km range, with no time delay. Introducing a 1 day delay between the electrons and the NO response, the positive correlation is found all the way down to 55 km. The highest correlation (0.85) occurs for altitudes 90–115 km after 1 day. For these altitudes, no significant correlation is found for delays more than 6 days. Farther down in the atmosphere, at 80–85 km, a positive correlation of 0.5 is also found with a 10–12 day delay. Below 65 km we see a positive correlation of about 0.5 with a 10 day delay, propagating down to 55 km after 15 days.

Using the POES data to estimate the production of NO and estimating photolysis losses as described in section 2.3, we obtain an approximation of accumulated NO. The correlation of the estimated accumulated NO with the NO change measured by SOFIE is shown in Figure 8 (right). The correlation is generally higher for all altitudes when accumulation and sunlight exposure is taken into account. At altitudes above 135 km, a

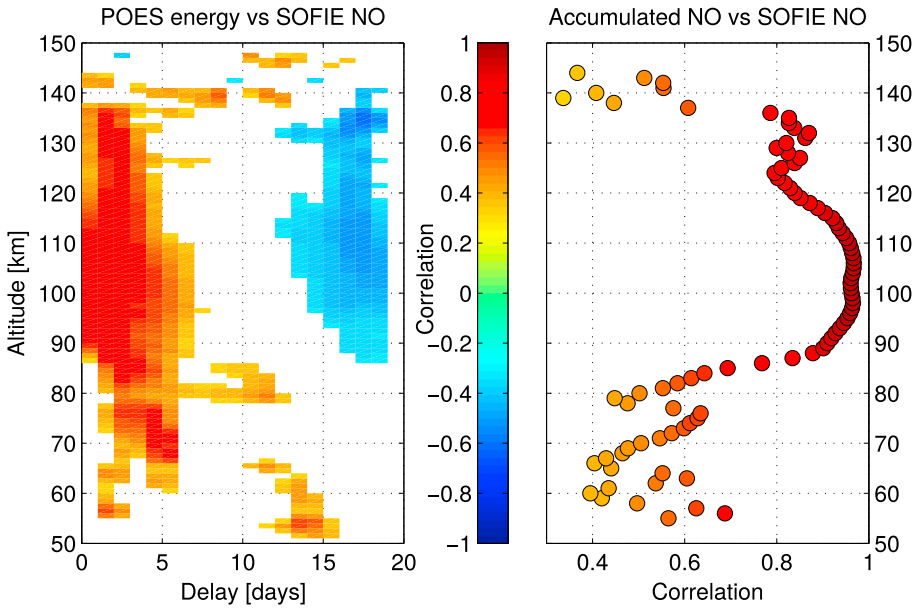

Figure 7. (left) Altitude profile of the Pearson correlation coefficient between SOFIE measurements of NO (relative change compared to climatology) and POES estimates of deposited energy. The correlation is done with a delay of 0–20 days between the energy deposition and the response in NO. Only correlation with 95% significance is shown. (right) Correlation between SOFIE measurements of NO (relative change compared to climatology) and POES estimates of accumulated NO, without any time delay. Only correlation with 95% significance is shown.

positive correlation of about 0.5 is found, increasing to 0.8 between 115 and 135 km. The highest correlation is also in this case found at altitudes between 90 and 115 km, reaching up to 0.97 with a 95% significance. Below 90 km, the correlation is lower but still significant, varying between 0.3 and 0.6 for altitudes between 55 km and 80 km. The accumulated NO estimate does not take horizontal or vertical transport into account, so the positive correlation found here is attributed only to the direct production and accumulation of NO.

4. Discussion

4.1. Direct Production

For the direct production of NO from EEP we expect a consistency between the electrons measured by POES and the NO number density observed by SOFIE, in terms of amount, timing, and latitudinal distribution.

To estimate if the observed increase could be due to direct production from electron precipitation, we compare it to the estimate of accumulated NO. Due to photolysis, the NO increase associated with the first event is expected to disappear before the second event starts. The NO number density is, however, still elevated and continues to be so for at least 2 weeks, which suggests that the indirect effect dominates after DOY 100. Based on the simple accumulated NO estimate, we expect NO increase on the scale of 10^9 cm^{-3} at 110 km, 10^8 at 100 km, and 10^7 at 90 km and between 10^{6-7} at 80 km and below. This is roughly in line with the increase found in the relative change of the measured NO, but there seems to be an apparent underestimate of the accumulated NO under 80 km altitude. The NO produced at lower altitudes is associated with medium-energy electrons which

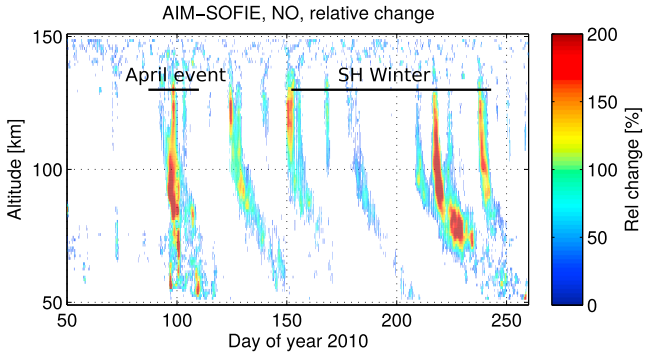

Figure 8. NO relative change in 2010 compared to 2008–2009/2011–2012 climatology. Only NO increase higher than one standard deviation of the climatology observations is shown. The geomagnetic storm period in April is highlighted, as well as the SH winter June, July, and August.

can have strongly anisotropic pitch angle distributions [*Rodger et al.*, 2013; *Nesse Tyssøy et al.*, 2016]. As we utilize only measurements from the 0° detector on MEPED, we are just including electrons with small pitch angles and we will underestimate the flux of precipitating electrons and then also the associated NO production. Looking at volume mixing ratio rather than number density (not shown), we can compare our results to *Sinnhuber et al.* [2014]. Relative to the climatology, we find an increase at DOY 96 in 2010 of 2 ppbv at 55 km, 3 ppbv at 60 km, and 5 ppbv at 65 km. This is in line with the *Sinnhuber et al.* [2014] findings during the October 2013 storm, that if there is a direct effect at 56–64 km, it is lower than 6 ppbv.

Comparing the timing of the observed NO increase to the deposited energy and accumulation estimate, we can also disentangle the direct and indirect effects. In the altitude region 90–115 km, we find an increase of the electron energy deposition already at DOY 92, which also is consistent with the observed NO. At the altitudes 55–80 km, an increase of electron flux is observed concurrent with the start of the event at DOY 95. Due to the accumulative effect, the maximum NO number density is expected to occur at DOY 96 at these altitudes. From the observed NO we see this increase at DOY 96 from 55 to 80 km as well. Hence, the timing of the observed NO is in agreement with the estimates of the accumulated direct effect. At and below 90 km we find two local maxima with respect to time. The most intense maximum occurs at all altitudes at DOY 96. The second maximum occurs at 55 km at about 15 days after the first CME. It is also evident that the enhancement persists longer at the lower altitudes in line with downward transport.

For the latitudinal extent, we expect a more structured NO from the direct effect than from the indirect effect, due to diffusion and advection. This is hard to confirm or invalidate due to the SOFIEs limited CGM latitudinal in the beginning of the event. It is, however, clear that the NO enhancement in the aftermath of the events spreads over a wider latitude band than typically associated with the auroral oval indicative of the indirect effect.

We find that both strength and timing give support for the NO increase all through the mesosphere to be associated with the direct effect. It is also clear that the altitudes 55–80 km are strongly impacted by the indirect effect. This assessment is further supported by the correlation analysis. At and above 90 km, the NO variations are well in line with the estimated accumulated NO abundance. The correlation coefficient is found to be between 0.8 at 90 km and 0.97 at 100 km suggesting that the direct effect is responsible for 65–95% of the variability. Below 80 km, the direct impact appears weaker, with a correlation coefficient between 0.3 and 0.6, suggesting that the direct effect is not the main contributor at these lower altitudes possible being responsible for only 10–35% of the variability throughout the event. This does not mean that vertical transport is responsible for the remaining variability as the correlation will also be reduced to horizontal transport.

4.2. Indirect Effect

In order to ascribe the main variability in NO number density to the vertical transport, realistic effective vertical descent rates and determination of altitude source region are essential to assess. At 55 km, the NO number density peaks around DOYs 108–110, about 15 days after the geomagnetic peak of the first CME event. The NO increase has a wide distribution in time and CGM latitude, typical for indirect events. We also find a poor correlation with the accumulated estimate of NO. Together, these features indicate that the NO increase at DOY 110 at 55 km is a result of the indirect effect. It remains to determine whether the initial source is the auroral electrons depositing their energy in the lower thermosphere or highly energetic electrons depositing their energy in the upper and middle mesosphere. The source is important to determine the delay between the electron precipitation event and the NO increase and subsequent impact on O_3 in the lower mesosphere and upper stratosphere. The source altitude is also essential to quantify the amount of NO that will reach a certain altitude, as a longer distance would lead to longer transport time and more of the initial produced NO will be lost due to diffusion and/or photolysis.

The effective downward transport of NO is the result of several processes, namely, large-scale advection, eddy and molecular diffusion, and chemical and photolytic losses, and differs from the actual mean atmospheric downward velocity, as represented by the transformed Eulerian mean velocity, for example, which is independent of the trace species considered [*Smith*, 2012; *Meraner and Schmidt*, 2016; *Orsolini et al.*, 2017]. Based on a NH model study with idealized tracer distributions, *Meraner and Schmidt* [2016] found that in early winter, under dynamically undisturbed conditions, molecular diffusion and advection are the dominant factors in the lower thermosphere giving an effective descent rate of 1.5 km/d while advection dominates below the mesopause, giving a rate of 0.5 km/d. Using NO observations from SOFIE, *Hendrickx et al.* [2015] found effective wintertime descent rates for NO of about 1 km/d for the NH and 1.2 km/d for SH, below 80–85 km. Using

carbon monoxide observations from the Microwave Limb Sounder, *Lee et al.* [2011] also found an effective descent rate in the SH—for that particular trace species—to be around 1 km/d near 80 km, decreasing by a factor 2 near 50 km. From the same SOFIE observations in the SH during the April 2010 EEP event, we find that the maximum NO density increases at 55 km about 15 days after it increased above 90 km. If NO had been descending from the level where the strongest changes are observed, near 90 km, the effective descent rate would be about 2.3 km/d. This unusually high descent rate suggests that the main source region is, during this event, at lower altitudes. Assuming an effective descent rate of 1.2 km/d, following the wintertime estimates in *Hendrickx et al.* [2015], places the source region at around 75 km, where we found also evidence for direct production. The advective term is likely to be even weaker in austral fall, when the mean meridional circulation builds up, and to decrease with height as well [*Lee et al.*, 2011], placing the source region even lower.

Previous studies suggest that the variability associated with the auroral electrons (<∼10 keV) are the most important source for the observed indirect impact in the upper stratosphere/lower mesosphere. Our case study implies that the medium-energy electrons (>∼10 keV) are most important for determining the NO variability at these altitudes. Previous studies have focused mainly on the winter season, where less photolysis will allow for a longer transport time compared to our event. Hence, our assessment of source region might be biased toward a lower source region.

In line with *Clilverd et al.* [2009] our study supports the conclusion that there could be significant direct contribution of the NO variability from the medium and relativistic electron precipitation. Previously, this has been thoroughly disputed by *Sinnhuber et al.* [2011] and *Funke et al.* [2007]. All of these studies investigated the complex winter of 2003/2004, where a sequence of solar proton events led to a high NO_x background and sudden stratospheric warming caused extraordinary dynamics associated with it, making it particularly hard to reveal a potential direct impact. On the other hand, *Kirkwood et al.* [2015] pointed out that there might be important NO production by medium and relativistic electrons, but it is hard to determine it in single case studies. Based on the particle measurements, we find the April event to be one of the strongest medium/relativistic electron event in the declining and minimum phase of the solar cycle. In addition, fall time might be favorable to reveal the direct effect compared to winter. During fall we have less photolysis compared to summer and the NO number density will accumulate so it is measurable above the background level. At the same time, the photolysis limits its effect in time enabling us to isolate the events to a larger degree than a pure winter study.

5. Conclusions

NOAA's multiple POES satellites enable us to construct polar maps of the precipitating electrons. By combining the low-energy electron channels from TED instrument with the high-energy channels from the MEPED instruments on the same satellites, we obtain a continuous energy spectrum ranging from 1 to 750 keV, which corresponds to atmospheric altitudes of 60–120 km. In Antarctic fall of 2010, a geomagnetic storm driven by a combination of a CIR and two CMEs occurred, resulting in both low and high energetic electrons precipitating into the atmosphere. The energy spectra of the incoming electron fluxes for this storm are compared to NO number density at 50–150 km altitude measured by the SOFIE instrument on board the NASA's AIM satellite.

We find evidence of direct production of NO down to 55 km. The medium-energy electrons (>10 keV) also contribute significantly to the indirect effect at these altitudes. The main source region for the indirect effect at 55 km altitude is estimated to be around ∼75 km following a typical descent rate of 1.2 km/d or ∼90 km following a relatively high descent rate of 2.3 km/d.

Acknowledgments
The research has been funded by the Norwegian Research Council, through project 222390, "Solar-Terrestrial Coupling through High Energy Particle Precipitation in the Atmosphere: A Norwegian contribution." L.M. and K.H. were supported by the Swedish Research Council under contract 621-2012-1648. H.N.T. and Y.O. were supported by the Norwegian Research Council under contract 223252/F50. We thank NOAA's National Geophysical Data Center (NGDC) for providing the NOAA POES data. The processed data used in this study are available upon request. The OMNI data were obtained from the GSFC/SPDF OMNIWeb interface at http://omniweb.gsfc.nasa.gov. The AIM-SOFIE data are found online at http://sofie.gats-inc.com/sofie/index.php.

References

Brasseur, G. P., and S. C. Solomon (2005), Aeronomy of the middle atmosphere: Chemistry and physics of the stratosphere, in *Atmospheric and Oceanographic Sciences Library*, vol. 32, 3rd ed., *Dynamics and transport*, chap. 3, pp. 51–149, Springer, Netherlands.

Clilverd, M. A., A. Seppälä, C. J. Rodger, M. G. Mlynczak, and J. U. Kozyra (2009), Additional stratospheric NO_x production by relativistic electron precipitation during the 2004 spring NO_x descent event, *J. Geophys. Res.*, *114*, A04305, doi:10.1029/2008JA013472.

Daae, M., P. J. Espy, H. Nesse Tyssøy, D. Newnham, J. Stadsnes, and F. Søraas (2012), The effect of energetic electron precipitation on middle mesospheric night-time ozone during and after a moderate geomagnetic storm, *Geophys. Res. Lett.*, *39*, L21811, doi:10.1029/2012GL053787.

Evans, D. S., and M. S. Greer (2000), Polar Orbiting Environmental Satellite space environment monitor—2. Instrument descriptions and archive data documentation, Tech. Rep., Natl. Atmos. and Oceanic Admin., Space Environ. Cent., Boulder, Colo.

Funke, B., M. Lopez-Puertas, S. Gil-Lopez, T. von Clarmann, G. P. Stiller, H. Fischer, and S. Kellmann (2005), Downward transport of upper atmospheric NO_x into the polar stratosphere and lower mesosphere during the Antarctic 2003 and Arctic 2002/2003 winters, *J. Geophys. Res.*, *110*, D24308, doi:10.1029/2005JD006463.

Funke, B., M. Lo, H. Fischer, G. P. Stiller, T. V. Clarmann, and G. Wetzel (2007), Comment on "Origin of the January–April 2004 increase in stratospheric NO_2 observed in northern polar latitudes" by Jean-Baptiste Renard et al., *Geophys. Res. Lett.*, *34*, L07813, doi:10.1029/2006GL027518.

Gonzalez, W. D., J. A. Joselyn, Y. Kamide, H. W. Kroehl, G. Rostoker, B. T. Tsurutani, and V. M. Vasyliunas (1994), What is a geomagnetic storm?, *J. Geophys. Res.*, *99*(A4), 5771–5792, doi:10.1029/93JA02867.

Gordley, L. L., et al. (2009), The solar occultation for ice experiment, *J. Atmos. Sol. Terr. Phys.*, *71*, 300–315, doi:10.1016/j.jastp.2008.07.012.

Hardy, D. A., M. S. Gussenhoven, and E. Holeman (1985), A statistical model of auroral electron precipitation, *J. Geophys. Res.*, *90*(A5), 4229–4248, doi:10.1029/JA090iA05p04229.

Hendrickx, K., L. Megner, J. Gumbel, D. E. Siskind, Y. J. Orsolini, H. Nesse Tyssøy, and M. Hervig (2015), Observation of 27 day solar cycles in the production and mesospheric descent of EPP-produced NO, *J. Geophys. Res. Space Physics*, *120*, 8978–8988, doi:10.1002/2015JA021441.

Holt, L. A., C. E. Randall, E. D. Peck, D. R. Marsh, A. K. Smith, and V. L. Harvey (2013), The influence of major sudden stratospheric warming and elevated stratopause events on the effects of energetic particle precipitation in WACCM, *J. Geophys. Res. Atmos.*, *118*, 11,636–11,646, doi:10.1002/2013JD020294.

Jackman, C. H., M. T. Deland, G. J. Labow, E. L. Fleming, D. K. Weisenstein, M. K. W. Ko, M. Sinnhuber, and J. M. Russell (2005), Neutral atmospheric influences of the solar proton events in October–November 2003, *J. Geophys. Res.*, *110*, A09S27, doi:10.1029/2004JA010888.

Kirkwood, S., and A. Osepian (2001), Pitch angle diffusion coefficients and precipitating electron fluxes inferred from EISCAT radar measurements at auroral latitudes, *J. Geophys. Res.*, *106*(A4), 5565–5578.

Kirkwood, S., A. Osepian, E. Belova, J. Urban, K. Pérot, and A. K. Sinha (2015), Ionization and NO production in the polar mesosphere during high-speed solar wind streams: Model validation and comparison with NO enhancements observed by Odin-SMR, *Ann. Geophys.*, *33*(5), 561–572, doi:10.5194/angeo-33-561-2015.

Laundal, K. M., and N. Østgaard (2009), Asymmetric auroral intensities in the Earths Northern and Southern hemispheres, *Nature*, *460*(7254), 491–493, doi:10.1038/nature08154.

Lee, J. N., D. L. Wu, G. L. Manney, M. J. Schwartz, A. Lambert, N. J. Livesey, K. R. Minschwaner, H. C. Pumphrey, and W. G. Read (2011), Aura Microwave Limb Sounder observations of the polar middle atmosphere: Dynamics and transport of CO and H_2O, *J. Geophys. Res.*, *110*, D05110, doi:10.1029/2010JD014608.

Loewe, C. A., and G. W. Prolls (1997), Classification and mean behaviour of magnetic storms, *J. Geophys. Res.*, *102*, 14,209–14,214.

López-Puertas, M., B. Funke, T. von Clarmann, H. Fischer, and G. P. Stiller (2006), The stratospheric and mesospheric NO_y in the 2002–2004 polar winters as measured by MIPAS/Envisat, *Space Sci. Rev.*, *125*, 403–416, doi:10.1007/s11214-006-9073-2.

Meraner, K., and H. Schmidt (2016), Transport of nitrogen oxides through the winter mesopause in HAMMONIA, *J. Geophys. Res. Atmos.*, *121*, 2556–2570, doi:10.1002/2015JD024136.

Mlynczak, M. G., L. A. Hunt, C. J. Mertens, B. T. Marshall, J. M. R. Russel, T. Woods, R. E. Thompson, and L. L. Gordley (2014), Influence of solar variability on the infrared radiative cooling of the thermosphere from 2002 to 2014, *Geophys. Res. Lett.*, *41*, 2508–2513, doi:10.1002/2014GL059556.

Nesse Tyssøy, H., M. I. J. Sandanger, L.-K. G. Ødegaard, J. Stadsnes, A. Aasnes, and A. E. Zawedde (2016), Energetic electron precipitation into the middle atmosphere—Constructing the loss cone fluxes from MEPED POES, *J. Geophys. Res. Space Physics*, *121*, 5693–5707, doi:10.1002/2016JA022752.

Newnham, D. A., P. J. Espy, M. A. Clilverd, C. J. Rodger, A. Seppälä, D. J. Maxfield, P. Hartogh, K. Holmén, and R. B. Horne (2011), Direct observations of nitric oxide produced by energetic electron precipitation into the Antarctic middle atmosphere, *Geophys. Res. Lett.*, *38*, L20104, doi:10.1029/2011GL048666.

Ødegaard, L.-K. G., H. Nesse Tyssøy, M. I. J. Sandanger, J. Stadsnes, and F. Søraas (2016), Space Weather impact on the degradation of NOAA POES MEPED proton detectors, *J. Space Weather Space Clim.*, *6*, A26.

Ødegaard, L. K. G., H. N. Tyssøy, J. Stadsnes, M. I. Sandanger, and F. Søraas (2017), Energetic electron precipitation in weak to moderate corotating interaction region-driven storms, *J. Geophys. Res. Space Physics*, *122*, 2900–2921, doi:10.1002/2016JA023096.

Orsolini, Y. J., V. Limpasuvan, K. Pérot, P. Espy, R. Hibbins, S. Lossow, K. Raaholt, and D. Murtagh (2017), Modelling the descent of nitric oxide during the elevated stratopause event of January 2013, *J. Atmos. Sol. Terr. Phys.*, *155*, 50–61, doi:10.1016/j.jastp.2017.01.006.

Randall, C. E., V. L. Harvey, C. S. Singleton, S. M. Bailey, P. F. Bernath, M. V. Codrescu, H. Nakajima, and J. M. Russell III (2007), Energetic particle precipitation effects on the Southern Hemisphere stratosphere in 1992–2005, *J. Geophys. Res.*, *112*, D08308, doi:10.1029/2006JD007696.

Randall, C. E., V. L. Harvey, L. A. Holt, D. R. Marsh, D. E. Kinnison, B. Funke, and P. F. Bernath (2015), Simulation of energetic particle precipitation effects during the 2003–2004 Arctic winter, *J. Geophys. Res. Space Physics*, *120*, 5035–5048, doi:10.1002/2015JA021196.

Rees, M. H. (1989), *Physics of the Upper Atmosphere, Cambridge Atmos. and Space Sci. Ser.*, Cambridge Univ. Press, Cambridge, U. K.

Renard, J.-B., P.-L. Blelly, Q. Bourgeois, M. Chartier, F. Goutail, and Y. J. Orsolini (2006), Origin of the January–April 2004 increase in stratospheric NO_2 observed in the northern polar latitudes, *Geophys. Res. Lett.*, *33*, L11801, doi:10.1029/2005GL025450.

Richardson, I. G., and H. V. Cane (2010), Near-Earth interplanetary coronal mass ejections during solar cycle 23 (1996–2009): Catalog and summary of properties, *Sol. Phys.*, *264*(1), 189–237, doi:10.1007/s11207-010-9568-6.

Richardson, I. G., and H. V. Cane (2017), Near-Earth interplanetary coronal mass ejections since January 1996. [Available at www.srl.caltech.edu/ACE/ASC/DATA/level3/icmetable2.htm.]

Rodger, C. J., A. J. Kavanagh, M. A. Clilverd, and S. R. Marple (2013), Comparison between POES energetic electron precipitation observations and riometer absorptions: Implications for determining true precipitation fluxes, *J. Geophys. Res. Space Physics*, *118*, 7810–7821, doi:10.1002/2013JA019439.

Rozanov, E., M. Calisto, T. Egorova, T. Peter, and W. Schmutz (2012), Influence of the precipitating energetic particles on atmospheric chemistry and climate, *Surv. Geophys.*, *33*(3–4), 483–501, doi:10.1007/s10712-012-9192-0.

Sandanger, M. I. J., L.-K. G. Ødegaard, H. Nesse Tyssøy, J. Stadsnes, F. Søraas, K. Oksavik, and K. Aarsnes (2015), In-flight calibration of NOAA POES proton detectors—Derivation of the MEPED correction factors, *J. Geophys. Res. Space Physics*, *120*, 9578–9593, doi:10.1002/2015JA021388.

Seppälä, A., P. T. Verronen, M. A. Clilverd, C. E. Randall, J. Tamminen, V. Sofieva, L. Backman, and E. Kyro (2007), Arctic and Antarctic polar winter NO_x and energetic particle precipitation in 2002–2006, *Geophys. Res. Lett.*, *34*, L12810, doi:10.1029/2007GL029733.

Sinnhuber, M., S. Kazeminejad, and J. M. Wissing (2011), Interannual variation of NO_x from the lower thermosphere to the upper stratosphere in the years 1991–2005, *J. Geophys. Res.*, *116*, A02312, doi:10.1029/2010JA015825.

Sinnhuber, M., H. Nieder, and N. Wieters (2012), Energetic particle precipitation and the chemistry of the mesosphere/lower thermosphere, *Surv. Geophys.*, *33*(6), 1281–1334, doi:10.1007/s10712-012-9201-3.

Sinnhuber, M., B. Funke, T. von Clarmann, M. López-Puertas, G. P. Stiller, and A. Seppälä (2014), Variability of NO_x in the polar middle atmosphere from October 2003 to March 2004: Vertical transport vs. local production by energetic particles, *Atmos. Chem. Phys.*, *14*, 7681–7692, doi:10.5194/acp-14-7681-2014.

Siskind, D. E., and J. M. Russell III (1996), Coupling between middle and upper atmospheric NO: Constraints from HALOE observations, *Geophys. Res. Lett.*, *23*(2), 137–140.

Smith, A. K. (2012), Interactions between the lower, middle and upper atmosphere, *Space Sci. Rev.*, *168*(1–4), 1–21, doi:10.1007/s11214-011-9791-y.

Tsurutani, B. T., and W. D. Gonzalez (1997), The interplanetary causes of magnetic storms: A review, in *Magnetic Storms, Geophys. Monogr. Ser.*, vol. 98, edited by B. T. Tsurutani et al., pp. 77–89, AGU, Washington, D. C., doi:10.1029/GM098p0077.

Verronen, P. T., and R. Lehmann (2013), Analysis and parameterisation of ionic reactions affecting middle atmospheric HO_x and NO_y during solar proton events, *Ann. Geophys.*, *31*, 909–956, doi:10.5194/angeo-31-909-2013.

Wissing, J. M., and M.-B. Kallenrode (2009), Atmospheric Ionization Module Osnabrück (AIMOS): A 3-D model to determine atmospheric ionization by energetic charged particles from different populations, *J. Geophys. Res.*, *114*, A06104, doi:10.1029/2008JA013884.

Yando, K. B., R. M. Millan, J. C. Green, and D. S. Evans (2011), A Monte Carlo simulation of the NOAA POES medium energy proton and electron detector instrument, *J. Geophys. Res.*, *116*, A10231, doi:10.1029/2011JA016671.

Erratum

In the originally published version of this article, the legends for Figures 7 and 8 were inadvertently transposed. This error has been corrected, and the present version may be considered the authoritative version of record.